Chemical Science

ROYAL SOCIETY OF CHEMISTRY

EDGE ARTICLE

View Article Online
View Journal

Cite this: DOI: 10.1039/d6sc02439d

All publication charges for this article have been paid for by the Royal Society of Chemistry

Synergistic Cu nanoparticles and Cu single atoms leveraging hydrogen spillover for selective CO electroreduction to acetate

Qinglong Wang,[ab] Tianfu Liu,*[ad] Xinhui Guo,[ad] Pengfei Wei,[ac] Dunfeng Gao,*[ad] Guoxiong Wang[ac] and Xinhe Bao[acd]

The electrochemical reduction of CO to acetate on Cu-based catalysts is constrained by a kinetic trade-off between CO activation and the availability of active hydrogen (*H) species. Herein, we overcome this limitation by constructing a synergistic catalyst comprising Cu nanoparticles and Cu single atoms (Cu_{NP}–Cu_1), which leverages a hydrogen spillover mechanism. The Cu_1 sites facilitate water dissociation to generate *H, which subsequently spills over to adjacent Cu NPs, enabling efficient hydrogenation of the *OCCO intermediate, with subsequent formation of *CCO selectively. This synergy delivers an acetate faradaic efficiency of 60.6% with an acetate partial current density of 111.1 mA cm^{-2} and stable operation for 132 h. *Operando* spectroscopy measurements and theoretical calculations collectively reveal that the Cu_1-mediated hydrogen spillover shifts the reaction pathway toward acetate formation. This work establishes hydrogen spillover as a design principle for coordinating multistep reactions in CO electroreduction.

Received 25th March 2026
Accepted 5th April 2026

DOI: 10.1039/d6sc02439d

rsc.li/chemical-science

Introduction

The electrochemical reduction of CO to multicarbon (C_{2+}) products represents a promising strategy for the sustainable production of high-value chemicals. Acetate, a key intermediate, finds extensive applications in fine chemicals, pesticides, fuels, and pharmaceuticals.[1,2] Although the formation of acetate is thermodynamically favorable, with a theoretical CO/acetate redox potential of 0.09 V *versus* the reversible hydrogen electrode (*vs.* RHE),[3] the catalytic process remains kinetically sluggish. The multi-proton–electron coupled transfer reaction poses a significant kinetic barrier, limiting the efficient conversion of CO to acetate.[4] To improve acetate selectivity, significant efforts have been focused on enhancing C–C coupling and increasing current density.[5–7] Strategies including optimizing crystal facets,[8,9] morphology,[10] interfaces,[11] and alloying[12–14] have been reported in recent years.

Cu stands out among metal catalysts owing to its unique ability to facilitate C–C coupling during CO electrochemical reduction, enabling the synthesis of valuable C_{2+} compounds.[15–17] Cu nanoparticles (NPs) exhibit favorable *CO adsorption thermodynamics and low C–C coupling barriers, making them efficient for generating C_{2+} products *via* *CO electroreduction.[18,19] As a result, Cu NPs typically enable appreciable formation of ethylene and ethanol.[20,21] However, the formation of the *OCCOH intermediate is widely recognized as a pivotal step in C_{2+} product generation, with its subsequent hydrogenation and dehydration *via* the ketene intermediate (*C=C=O) selectively driving the reaction pathway toward acetate formation, which is kinetically constrained by the limited availability of active hydrogen (*H) species on Cu surfaces.[22–25]

Hydrogen spillover has emerged as a key mechanism to regulate interfacial *H abundance, lowering the energy barrier for C–C coupling.[26,27] Recently, single-atom Cu catalysts (Cu_1) have been shown to facilitate water dissociation for efficient *H generation, promoting the conversion of *CO to *CHO.[28] It is widely reported that the synergistic increase in the *H and *CO surface coverage kinetically steers the reaction pathway toward asymmetric C–C coupling *via* preferential *CO hydrogenation.[29–31] In such a scenario, synergistic catalysis is expected to be a feasible strategy to balance the *CO adsorption and the hydrogenation kinetics of carbon intermediates.

Herein, we construct a synergistic catalyst by introducing Cu single atoms onto Cu NPs (Cu_{NP}–Cu_1) for electrochemical CO reduction to acetate, with a faradaic efficiency of 60.6%, a partial current density of 111.1 mA cm^{-2} and durability for 132 hours. Electrochemical CO stripping experiments, *operando*

[a]State Key Laboratory of Catalysis, Dalian Institute of Chemical Physics, Chinese Academy of Sciences, Dalian 116023, China. E-mail: ltianfu@dicp.ac.cn; dfgao@dicp.ac.cn

[b]Key Laboratory of Green Chemical Process of Ministry of Education, Hubei Key Laboratory of Novel Reactor and Green Chemical Technology, School of Chemical Engineering and Pharmacy, Wuhan Institute of Technology, Wuhan 430205, China

[c]Department of Chemistry, Shanghai Key Laboratory of Molecular Catalysis and Innovative Materials, iChEM (Collaborative Innovation Center of Chemistry for Energy Materials), Fudan University, Shanghai 200438, China

[d]University of Chinese Academy of Sciences, Beijing 100049, China

Raman spectroscopy and H/D kinetic isotope effect (KIE) studies reveal that Cu NPs facilitate C–C coupling by effectively adsorbing CO molecules and Cu single atoms enhance the dissociation of H_2O to generate active *H species, promoting hydrogen spillover from Cu_1 sites to Cu_{NP}. Density functional theory (DFT) calculations incorporating *ab initio* molecular dynamics (AIMD) simulations indicate that the modulated *H coverage thermodynamically drives the formation of key intermediates, ultimately enhancing acetate production. This work establishes hydrogen spillover engineering as a general strategy to coordinate multistep reactions in CO electroreduction systems.

Results and discussion

Structural and morphological characterization

The Cu_{NP}–Cu_1 catalyst was synthesized *via* the pyrolysis of a Cu coordination polymer under Ar flow (Fig. S1). The scanning electron microscopy (SEM) image, as illustrated in Fig. 1a, reveals a smooth and granular texture. The transmission electron microscopy (TEM) image of Cu_{NP}–Cu_1 (Fig. 1b) reveals the presence of Cu NPs (Cu_{NP}) with an average size of 3.1 nm within the Cu_{NP}–Cu_1 catalyst (see SEM and TEM images in Fig. S2). Aberration-corrected high-angle annular dark-field scanning transmission electron microscopy (HAADF-STEM) images (Fig. 1c) reveal that Cu single atoms (highlighted by red circles) are densely dispersed around Cu nanoparticles with an average inter-site distance of approximately 0.22 nm (Fig. S3). Such atomic-level spatial proximity is essential for efficient hydrogen spillover, as it minimizes the migration distance of *H species between Cu_1 and Cu_{NP} surfaces.[32] A lattice spacing of 0.20 nm for the Cu_{NP} is consistent with the (111) crystal plane of metallic Cu, confirmed by the intensity profile derived from the STEM image (Fig. 1d). For comparison purposes, we prepared $2Cu_{NP}$–Cu_1 (doubled copper salt, Fig. S4), Cu NPs (Cu nanoparticles loaded on XC72R, Fig. S5a) and CuSA (Cu single atom, Cu_{NP}–Cu_1 etched with H_2SO_4 to remove Cu_{NP}, Fig. S5b and c). X-ray diffraction (XRD) patterns of Cu_{NP}–Cu_1, and Cu NPs (Fig. 1e) show characteristic peaks attributed to metallic copper and carbon, with a prominent peak at 43.2° corresponding to the Cu (111) plane. In contrast, the XRD pattern of CuSA exhibited typical diffraction patterns of amorphous carbon, with no discernible peaks attributable to copper. Energy-dispersive X-ray spectroscopy (EDS) elemental mapping (Fig. 1f) indicates a uniform distribution of C, N, and Cu on the carbon matrix, suggesting that these elements are evenly dispersed.

To further elucidate the precise coordination structure and chemical state of Cu within the catalyst, X-ray absorption near-edge structure (XANES) and extended X-ray absorption fine structure (EXAFS) characterization studies were employed. Fig. 2a shows the Cu K-edge XANES spectra of Cu_{NP}–Cu_1, $2Cu_{NP}$–Cu_1, Cu foil, and CuPc. The absorption edge position for Cu_{NP}–Cu_1 lies between those of Cu foil and CuPc, indicating that the average oxidation state of Cu in the catalyst is between

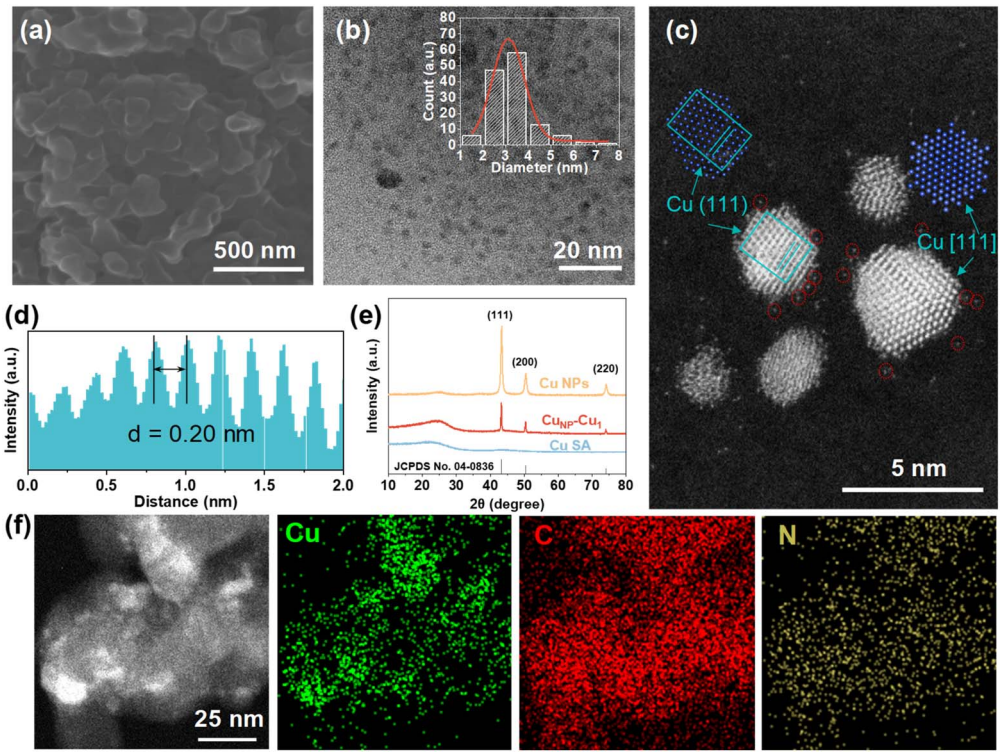

Fig. 1 (a) SEM and (b) TEM images of the Cu_{NP}–Cu_1 catalyst. (c) Aberration-corrected HAADF-STEM image of the Cu_{NP}–Cu_1 catalyst (the blue lattices represent the crystal model formed by expanding the unit cell of FCC copper into a 3 × 3 × 3 supercell). (d) Intensity profiles measured from HAADF-STEM images of the Cu_{NP}–Cu_1 catalyst. (e) XRD patterns of Cu NPs, Cu_{NP}–Cu_1 and CuSA. (f) EDS elemental maps of the Cu_{NP}–Cu_1 catalyst.

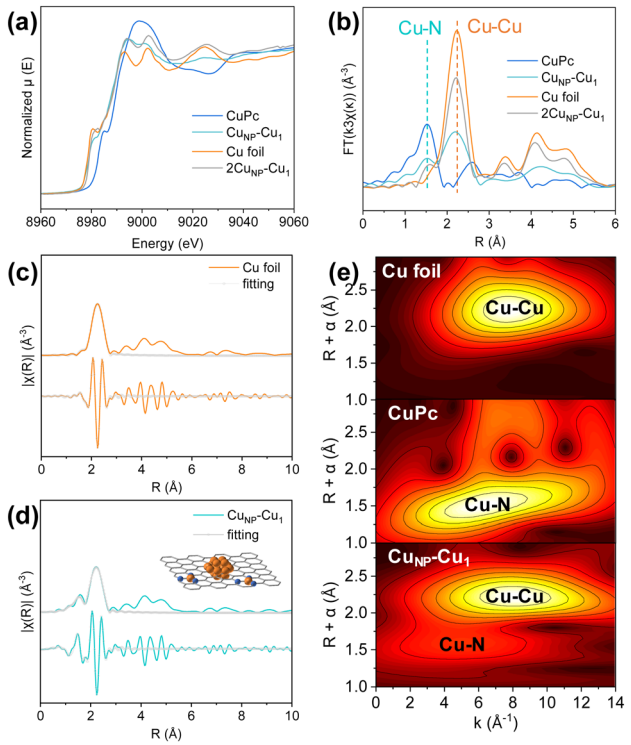

Fig. 2 (a) Cu K-edge XANES spectra of Cu_{NP}–Cu_1 and $2Cu_{NP}$–Cu_1, in comparison to Cu foil and CuPc. (b) Fourier-transform (FT)-EXAFS spectra of Cu_{NP}–Cu_1, $2Cu_{NP}$–Cu_1, Cu foil and CuPc. FT-EXAFS spectral fittings for (c) Cu foil and (d) the Cu_{NP}–Cu_1 catalyst. (e) Wavelet-transform (WT)-EXAFS of Cu_{NP}–Cu_1, CuPc and Cu foil at the Cu K-edge.

0 and +2. This suggests the coexistence of Cu^0 and Cu^{2+} species within the Cu_{NP}–Cu_1 catalyst. The Fourier transform (FT) EXAFS spectra in *R*-space, shown in Fig. 2b, reveal distinct features. Cu foil exhibits a characteristic first shell Cu–Cu bond at 2.2 Å, while CuPc shows a Cu–N bond at 1.5 Å. In contrast, Cu_{NP}–Cu_1 and $2Cu_{NP}$–Cu_1 display two bond lengths at 1.5 Å and 2.2 Å, corresponding to Cu–N and Cu–Cu bonds, respectively.[33,34] The Fourier-transformed EXAFS fitting plots and k^3-weighted Cu K-edge EXAFS spectra of Cu foil and Cu_{NP}–Cu_1 catalysts demonstrate a good fitting quality of the EXAFS data (Fig. 2c, d and S6). Additionally, wavelet transform (WT)-EXAFS analysis was conducted on the Cu K-edge of Cu_{NP}–Cu_1, Cu foil, and CuPc (Fig. 2e). Cu foil exhibits a maximum WT intensity at $k = 7.0$ Å^{-1}, indicative of Cu–Cu coordination, whereas CuPc shows a maximum WT intensity at $k = 6.0$ Å^{-1}, corresponding to Cu–N coordination. Notably, Cu_{NP}–Cu_1 presents maxima at both $k = 6.0$ Å^{-1} and $k = 7.0$ Å^{-1}, confirming the presence of both Cu–Cu and Cu–N bonds. The EXAFS fitting yields an average Cu–N coordination number of 2.7, consistent with a distribution of coordination environments where Cu–N_3 is the dominant motif (Table S1). DFT calculations based on a representative Cu–N_3 model were employed to elucidate the mechanistic role of the Cu single-atom sites. This evidence further corroborates the coexistence of Cu single atoms and Cu NPs in Cu_{NP}–Cu_1, aligning with HAADF-STEM observations.

Electrochemical CO reduction performance

The electrochemical performance of Cu_{NP}–Cu_1 was evaluated in a flow cell (Fig. S7). Fig. S8 shows a notable increase in cathodic current density when the feed gas was switched from Ar to CO. The mass loading of the Cu_{NP}–Cu_1 catalyst on carbon paper was optimized to assess CO reduction reaction (CORR) performance. As shown in Fig. 3a and S9, the catalyst with a mass loading of 0.5 mg cm^{-2} led to a prominent acetate partial current density. The catalytic performance of Cu_{NP}–Cu_1 was benchmarked against Cu NPs and CuSA under identical conditions (Fig. 3a–e). Notably, the faradaic efficiency (FE) for acetate over the Cu_{NP}–Cu_1 catalyst reaches 57.6% at −1.24 V *vs.* RHE with a partial current density of 103.9 mA cm^{-2}. In contrast, the sum of acetate FE from Cu NPs (FE ~20%) and CuSA (FE ~10%) individually is substantially lower than that of Cu_{NP}–Cu_1, providing a clear indication of synergistic enhancement rather than simple additive effects (Fig. 3a–d). The partial current densities of acetate and C_{2+} products on Cu_{NP}–Cu_1, Cu NPs, and CuSA show a sustained increase as the applied potential shifts negatively (Fig. 3d and e). The faradaic efficiency for C_{2+} products on Cu_{NP}–Cu_1 reaches 83.4% with a partial current density of 150.5 mA cm^{-2} (Fig. 3e and S10). The carbon selectivity distribution among CO electrolysis products exhibits pronounced disparities in carbonaceous product formation. Cu_{NP}–Cu_1 demonstrates an exceptional acetate selectivity of approximately 80%, whereas Cu NPs and CuSA catalysts show substantial reductions in acetate production efficiency (Fig. S11). Moreover, commercial Cu NPs (25 nm) also exhibit a product distribution similar to Cu NPs (Fig. S12).

To further probe the origin of this synergy, we systematically varied the Cu_{NP}/Cu_1 ratio by quantifying CuSA and Cu NPs in the 2CuSA, CuSA, 0.5CuSA, Cu_{NP}–Cu_1, $2Cu_{NP}$–Cu_1 and $0.5Cu_{NP}$–Cu_1 catalysts by inductively coupled plasma-optical emission spectrometry (ICP-OES) measurements (Table S2) and evaluated their CORR performance (Fig. S13). A volcano-shaped relationship emerges between the Cu_{NP}/Cu_1 ratio and acetate FE, with the optimal performance centered at Cu_{NP}–Cu_1. Catalysts with insufficient Cu_1 sites suffer from limited *H supply, while those with excessive Cu_1 sites exhibit diminished C–C coupling due to insufficient Cu NP surfaces. This volcano trend underscores the necessity of balancing the *CO activation and the *H generation for selective acetate formation. These results confirm that the selective acetate formation is a result of the synergistic effect between Cu nanoparticles and Cu single atoms. Additionally, electrochemical impedance spectroscopy (EIS) and double-layer capacitance (C_{dl}) measurements indicate that the coexistence of Cu nanoparticles and single atoms accelerates electron transfer within Cu_{NP}–Cu_1 and provides more active sites (Fig. S14 and S15).

To further investigate the role of *CO coverage in steering product selectivity, we evaluated the CO electroreduction performance of Cu_{NP}–Cu_1 in an alkaline membrane electrode assembly (MEA) electrolyzer under both 0.1 and 1.0 MPa CO. As illustrated in Fig. 3f and S16, at 0.1 MPa CO, the acetate FE reaches 48.5%, with partial current densities of 184.7 mA cm^{-2} for C_{2+} products and 94.8 mA cm^{-2} for acetate. Upon increasing the CO pressure to 1.0 MPa, the acetate FE markedly increases

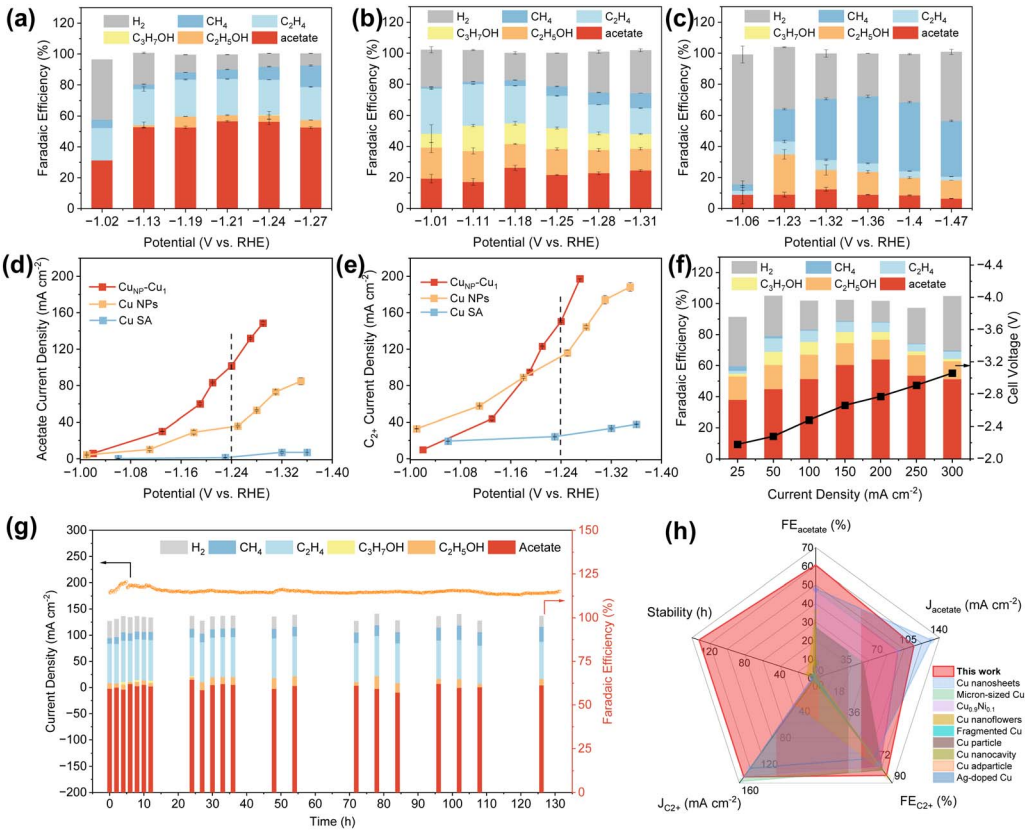

Fig. 3 Faradaic efficiency of products over (a) Cu_{NP}–Cu_1, (b) Cu NPs and (c) the CuSA catalyst in 1.0 M KOH electrolyte. (d) Acetate and (e) C_{2+} current densities as a function of potential over Cu_{NP}–Cu_1, Cu NPs, and CuSA. (f) Faradaic efficiency of products and cell voltages for the Cu_{NP}–Cu_1 catalyst at 1.0 MPa CO partial pressure in an MEA electrolyzer. (g) Long-term stability of Cu_{NP}–Cu_1 at a potential of −1.24 V *vs.* RHE in 1.0 M KOH electrolyte. (h) Comparison of this work with the literature benchmarks for CORR electrodes, including acetate/C_{2+} partial current density, acetate/C_{2+} FE, and operation stability.

to 64.0%, and the corresponding partial current density increases to 127.9 mA cm^{-2}. This pronounced shift in product distribution provides strong experimental evidence for the proposed synergy between *CO coverage and hydrogen spillover. Elevated CO pressure significantly increases *CO surface coverage on Cu nanoparticles, which not only promotes C–C coupling kinetics but also synergizes with the high *H coverage sustained by hydrogen spillover from adjacent Cu single atoms. These pressure-dependent results thus independently validate the proposed hydrogen spillover mechanism, confirming that the synergy between *CO coverage and *H supply dictates product selectivity.[35–37]

Furthermore, the durability test conducted at −1.24 V *vs.* RHE reveals that the Cu_{NP}–Cu_1 catalyst remains stable for 132 hours without obvious current decay, maintaining an average acetate faradaic efficiency of 60.6% and an average current density of 111.1 mA cm^{-2} (Fig. 3g). Compared with literature benchmarks, this work outperforms state-of-the-art CORR electrodes in terms of acetate partial current density and operation stability (Fig. 3h and Table S3).

Mechanistic investigation of hydrogen spillover

We characterized the structural changes in the catalyst using quasi *in situ* X-ray photoelectron spectroscopy (XPS) under oxygen-free conditions to accurately determine the oxidation state of Cu during CO electroreduction. The Cu 2p spectrum (Fig. 4a) reveals peaks corresponding to metallic Cu (Cu^0) at 932.8 eV and single-atom Cu (Cu^{2+}) at 934.6 eV for Cu $2p_{3/2}$.[38,39] After performing CO electroreduction at 150 mA cm^{-2} in a 1.0 M KOH solution, the single-atom Cu in the catalyst is partially reduced to metallic copper. The N 1s spectrum (Fig. 4b) indicates the presence of pyridinic N at 398.7 eV and pyrrolic N at 400.8 eV. Additionally, a Cu–N peak observed near 399.8 eV suggests coordination between copper sites and nitrogen atoms.[40,41] The decrease in the proportion of pyridinic N after the reaction may be attributed to the breaking of Cu–N bonds during the reaction, leading to the release of single-atom copper. As shown in Fig. 4c, nonlinear least squares fitting (NLLSF) of the Cu LMM Auger spectrum further confirms the coexistence of Cu^{2+} and Cu^0, with kinetic energies of 917.2 eV and 919.4 eV, respectively.[42–44] The catalyst surface contains a higher abundance of single-atom Cu before the CORR than that after the reaction. Although minor coarsening of the Cu_{NP} is observed in Fig. S17, this structural modification has no detrimental effects on the CORR catalytic performance based on long-term stability results and the unchanged contact angle (Fig. S18). Taken together, these findings demonstrate that the Cu_{NP}–Cu_1 architecture maintains structural integrity through

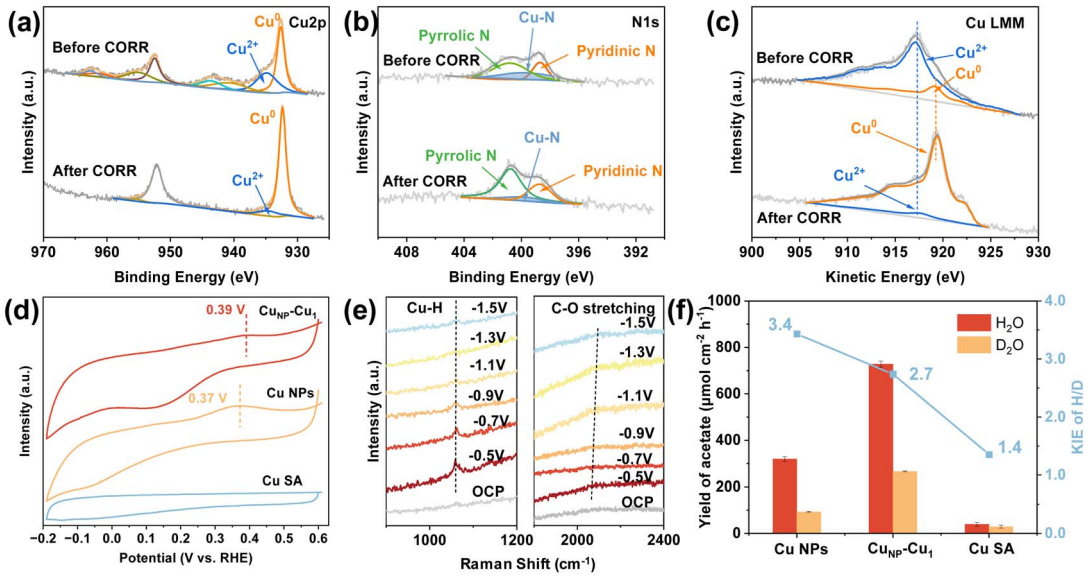

Fig. 4 Quasi *in situ* XPS spectra of (a) Cu 2p and (b) N 1s of the Cu_{NP}–Cu_1 catalyst in the as-prepared state and after the CO reduction reaction (CORR) at 150 mA cm^{-2}. (c) Non-linear least squares fitting (NLLSF) of Cu LMM. (d) The electrochemical CO stripping voltammetry tests of Cu_{NP}–Cu_1, Cu NPs and CuSA in 0.2 M K_2SO_4 electrolyte. (e) *Operando* Raman spectra of the Cu_{NP}–Cu_1 catalyst. (f) The H/D kinetic isotope effect (KIE) on Cu_{NP}–Cu_1 and CuSA catalysts in 1.0 M KOH electrolyte.

adaptive restructuring during prolonged electrochemical operation.

Electrochemical CO stripping voltammetry tests were conducted to evaluate the CO adsorption performance of Cu_{NP}–Cu_1, Cu NPs, and CuSA in a flow cell. The CO desorption peaks for Cu_{NP}–Cu_1 and Cu NPs are located at 0.39 and 0.37 V, respectively, indicating strong CO adsorption on the Cu_{NP}–Cu_1 catalyst (Fig. 4d). No CO desorption peaks were observed for catalysts without adsorbing CO (Fig. S19). A higher CO desorption potential indicates stronger CO adsorption ability.[45,46] Cu SA shows no detectable CO desorption peak, confirming that Cu NPs are the primary sites for *CO activation. This functional separation is the prerequisite for the proposed synergistic mechanism. To probe surface species evolution on Cu_{NP}–Cu_1 during the CORR, *operando* Raman spectroscopy was employed. As depicted in Fig. 4e, spectra acquired from −0.5 to −1.5 V *vs.* RHE exhibit two characteristic bands, the peak at 1060 cm^{-1} corresponding to Cu–H bending vibrations,[47] and the band at 2080 cm^{-1} assigned to atop-adsorbed *CO (C≡O stretching).[35,48] The inverse intensity correlation, that is, a decreasing Cu–H signal with increasing *CO adsorption, reveals consumption of adsorbed hydrogen species during CO adsorption at cathodic potentials.[49] In contrast, control experiments with the Cu NP catalyst show no detectable *CO or Cu–H signals until more negative potentials (Fig. S20), demonstrating that Cu_1 sites critically enhance both *CO adsorption and hydrogen spillover kinetics on adjacent Cu_{NP} surfaces.

To investigate the role of Cu_1 in water dissociation, the H/D KIE experiments were conducted. When D_2O replaces H_2O in the electrolyte, the production rates of products decrease for Cu_{NP}–Cu_1, Cu NPs, and CuSA catalysts. The magnitude of this decrease was closely correlated with the ratio of Cu_{NP} to Cu_1 content. The KIE of H/D is defined as the ratio of production rates in H_2O and D_2O electrolytes. A KIE value close to 1 indicates minimal impact of water dissociation on product formation, whereas a larger KIE suggests a significant influence of hydrogen spillover on the production rate.[28,29] A calibration curve between the concentration of deuterated acetate and deuterated dimethyl sulfoxide (DMSO) was plotted to quantify acetate-d (Fig. S21 and S22). As shown in Fig. 4f, the KIE value for acetate production on Cu SA is 1.4, close to unity, indicating that water dissociation is not rate-limiting. In contrast, Cu NPs exhibit a KIE of 3.4, suggesting that *H supply substantially limits acetate formation on pure Cu NPs. Cu_{NP}–Cu_1 displays a moderate KIE of 2.7, consistent with Cu_1 sites accelerating water dissociation and supplying *H to Cu NPs. Besides, KIE values for C_2H_4 and H_2 yield present similar trends to that of acetate (Fig. S23). An increase in Cu_1 content within the catalysts accelerates the water dissociation rate, leading to a decrease in the KIE value. The integration of Cu_1 into Cu_{NP} amplifies the KIE value for C_{2+} formation, confirming that Cu_1-mediated hydrogen spillover occurs between Cu_1 and Cu_{NP}.

DFT calculations

DFT calculations incorporating AIMD simulations were conducted to mechanistically decode the dual-site synergy in the CO electroreduction pathway. The investigation focuses on the H_2O dissociation kinetics for the hydrogen source and C–C coupling. The computational models Cu(100) and Cu–N_3 moiety were constructed to model Cu_{NP} and Cu_1 sites.[50,51] To identify the primary source of *H supply, we calculated the free energy profiles for H_2O dissociation on both sites using AIMD simulations. The reaction coordinate Δd was defined to track the O–H bond scission, which was expressed as the difference

between the forming and breaking bond lengths: $\Delta d = d_{H\text{–}Cu} - d_{H\text{–}O}$ on Cu_{NP}, and $\Delta d = d_{H\text{–}N} - d_{H\text{–}O}$ on Cu_1 sites[52] (Fig. 5a, b, S24 and S25). The results revealed a clear distinction between the two sites. The energy barrier on Cu(100) increased inversely with Δd, reaching 1.38 eV at the final state of H_2O dissociation. The Cu–N_3 site exhibited a dramatically lower barrier of 0.13 eV, indicating kinetically favorable water dissociation. This direct comparison demonstrates that Cu_1 sites reduce the H_2O dissociation barrier by 1.25 eV relative to Cu_{NP}, confirming that the single-atom sites are the kinetically favorable centers for generating *H species. This theoretical insight aligns with experimental *operando* Raman spectroscopy and KIE values, corroborating the synergistic mechanism wherein Cu_1 sites efficiently generate *H, which then spills over to adjacent Cu_{NP} surfaces to facilitate the hydrogenation of key intermediates within the overall CORR pathway.

Given the established significance of the *OCCOH to ketene pathway as selectivity-determining for acetate production, the energetics of *OCCOH formation can be considered a key descriptor for a catalyst's C–C coupling performance and overall C_{2+} selectivity. We therefore systematically investigated the impact of *H coverage on this crucial step.[53] DFT calculations uncovered a coverage-dependent energetic switching behavior. *OCCOH formation becomes increasingly endergonic (ΔG up to 1.33 eV) at low *H coverage ($\theta_H \leq 1/2$ ML). However, at high *H coverage ($\theta_H = 3/4$ ML), the reaction barrier is dramatically reduced to 1.02 eV (Fig. 5c, S26 and Table S4), enabling the pathway kinetically accessible under operational potentials. These computational insights demonstrate that high *H coverage (>1/2 ML) is favorable for *OCCOH formation, indicating that a high *H concentration is crucial for promoting the overall reaction pathway towards C_{2+} products. As shown in Fig. 5d and Table S4, the energy of the acetate intermediate *CCO at 3/4 ML coverage is −1.64 eV, which is lower than −1.09 eV at 0 ML coverage. In contrast, the energy of the ethylene intermediate *COHCOH at 3/4 ML coverage is −0.41 eV, higher than −0.61 eV at 0 ML coverage. Since a more negative energy indicates a more favorable process, acetate formation becomes more favorable at high *H coverage. This coverage-dependent energetics explains that Cu_1-mediated hydrogen spillover directs the selectivity toward acetate over ethylene.

Collectively, our experimental and theoretical results converge on a unified mechanistic picture. Cu_1 sites in the

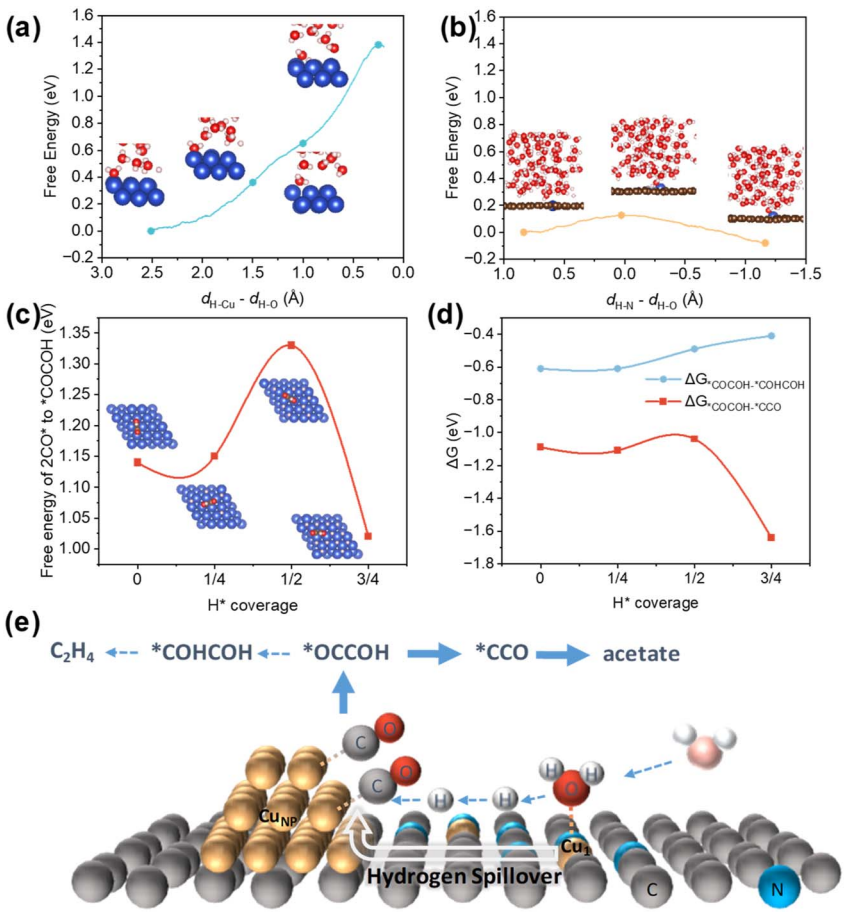

Fig. 5 Free energy profiles and representative structures for H_2O dissociation with different Δd over (a) Cu and (b) Cu–N_3. (c) Reaction energy of *COCOH formation over Cu as a function of *H coverage. Cu, O, H, and N elements are represented by blue, red, pink and grey spheres. (d) Reaction energy of *COCOH to *CCO and *COCOH to *COHCOH over Cu as a function of *H coverage. (e) Schematic diagram of the proposed mechanism for the CORR to acetate on Cu_{NP}–Cu_1.

Cu_{NP}–Cu_1 catalyst function as *H flux amplifiers to accelerate water dissociation and enable hydrogen spillover onto adjacent Cu_{NP}, where *CO is activated (Fig. 5e). The resulting high *H coverage on Cu NPs selectively promotes *OCCO hydrogenation toward acetate, circumventing the kinetic trade-off inherent in conventional Cu catalysts. This mechanism dynamically enhances acetate selectivity by 2.7-fold and 6.5-fold *versus* Cu_{NP}-only and Cu_1-only catalysts, respectively.

Conclusions

In summary, we have demonstrated that the spatial integration of Cu nanoparticles and Cu single atoms enables a hydrogen spillover mechanism that decouples the kinetic trade-off between CO activation and *H supply in CO electroreduction. The Cu_1 sites accelerate water dissociation to form *H, while the proximal Cu NPs enable the *H-assisted C–C coupling and acetate pathway. This synergy results in impressive acetate selectivity and operation stability, and more importantly, establishes hydrogen spillover as a general strategy for coordinating multistep reactions in complex electrocatalytic systems.

Author contributions

Conceptualization: D. G. and T. L.; methodology: Q. W., T. L., X. G., P. W., and D. G.; investigation: Q. W. and T. L.; visualization: Q. W. and T. L.; funding acquisition: G. W., D. G., T. L., and Q. W.; supervision: D. G., T. L., G. W., and X. B.; writing—original draft: Q. W. and T. L.; writing—review and editing: D. G., T. L., G. W., and X. B.

Conflicts of interest

The authors declare no conflict of interest.

Data availability

The data underlying this article are available in the article and in its online supplementary information (SI). Supplementary information: experimental and theoretical details as well as additional characterization and performance data. See DOI: https://doi.org/10.1039/d6sc02439d.

Acknowledgements

This work was supported by the National Key Research and Development Program of China (2021YFA1501500), the National Natural Science Foundation of China (22372171, 22472176, 22494711, 22125205, and 22321002), the Strategic Priority Research Program of the Chinese Academy of Sciences (XDB0600200), the Liaoning Revitalization Talents Program (XLYC2203178), the Liaoning Binhai Laboratory (LBLF-2023-02, LBLD-2024-02), the Natural Science Foundation of Liaoning Province (2026JH6/101100020), the Dalian Outstanding Young Scientist Foundation (2024RJ003), the Dalian Institute of Chemical Physics (DICP I202504), the China Postdoctoral Science Foundation (2023M743427), the Postdoctoral Fellowship Program of CPSF (GZC20232586), and the Photon Science Center for Carbon Neutrality (JZHKYPT-2021-07). We thank the Shanghai Synchrotron Radiation Facility of BL14W1 (https://cstr.cn/31124.02.SSRF.BL14W1) for assistance in XAS measurements.

Notes and references

1 J. Y. T. Kim, C. Sellers, S. Hao, T. P. Senftle and H. Wang, *Nat. Catal.*, 2023, **6**, 1115–1124.
2 W. Ma, X. He, W. Wang, S. Xie, Q. Zhang and Y. Wang, *Chem. Soc. Rev.*, 2021, **50**, 12897–12914.
3 H. Du, J. Fu, L.-X. Liu, S. Ding, Z. Lyu, Y.-C. Chang, X. Jin, F. O. Kengara, B. Song, Q. Min, J.-J. Zhu, D. Du, C. Gu, Y. Lin, J.-S. Hu and W. Zhu, *Mater. Today*, 2022, **59**, 182–199.
4 Y. Zhao, Y. Li, J. Chen, B. Sun, L. Fan, J. Chen, Y. Xiao, H. Yang, D. Wang, J. Chen, X. Han, S. Xi, J. Zhang and L. Wang, *ACS Catal.*, 2024, **14**, 8366–8375.
5 J. Wu, T. Sharifi, Y. Gao, T. Zhang and P. M. Ajayan, *Adv. Mater.*, 2019, **31**, 1804257.
6 T. Wang, Q. Zhao, Y. Fu, C. Lei, B. Yang, Z. Li, L. Lei, G. Wu and Y. Hou, *Small Methods*, 2019, **3**, 1900210.
7 N. Meng, Z. Wu, Y. Huang, J. Zhang, M. Chen, H. Ma, H. Li, S. Xi, M. Lin, W. Wu, S. Han, Y. Yu, Q.-H. Yang, B. Zhang and K. P. Loh, *Nat. Commun.*, 2024, **15**, 3892.
8 J. Liu, Y. Wen, W. Yan, Z. Huang, X. Liu, X. Huang, C. Zhan, Y. Zhang, W.-H. Huang, C.-W. Pao, Z. Hu, D. Su, S. Xie, Y. Wang, J. Han, H. Xiong, X. Huang and N. Chen, *Energy Environ. Sci.*, 2025, **18**, 4396–4404.
9 Z.-Z. Wu, X.-L. Zhang, Z.-Z. Niu, F.-Y. Gao, P.-P. Yang, L.-P. Chi, L. Shi, W.-S. Wei, R. Liu, Z. Chen, S. Hu, X. Zheng and M.-R. Gao, *J. Am. Chem. Soc.*, 2022, **144**, 259–269.
10 P. Zhu, C. Xia, C.-Y. Liu, K. Jiang, G. Gao, X. Zhang, Y. Xia, Y. Lei, H. N. Alshareef and T. P. Senftle, *Proc. Natl. Acad. Sci. U. S. A.*, 2021, **118**, e2010868118.
11 W. Wei, Z. Li, J. Shang, C. Xia, X. Hu, Y. Hu, J. Xu, Y. Zhao and M. Ding, *Appl. Catal., B*, 2025, **371**, 125220.
12 Y. Ji, Z. Chen, R. Wei, C. Yang, Y. Wang, J. Xu, H. Zhang, A. Guan, J. Chen, T.-K. Sham, J. Luo, Y. Yang, X. Xu and G. Zheng, *Nat. Catal.*, 2022, **5**, 251–258.
13 J. Jin, J. Wicks, Q. Min, J. Li, Y. Hu, J. Ma, Y. Wang, Z. Jiang, Y. Xu, R. Lu, G. Si, P. Papangelakis, M. Shakouri, Q. Xiao, P. Ou, X. Wang, Z. Chen, W. Zhang, K. Yu, J. Song, X. Jiang, P. Qiu, Y. Lou, D. Wu, Y. Mao, A. Ozden, C. Wang, B. Y. Xia, X. Hu, V. P. Dravid, Y.-M. Yiu, T.-K. Sham, Z. Wang, D. Sinton, L. Mai, E. H. Sargent and Y. Pang, *Nature*, 2023, **617**, 724–729.
14 Q. Sun, Y. Zhao, X. Tan, C. Jia, Z. Su, Q. Meyer, M. I. Ahmed and C. Zhao, *ACS Catal.*, 2023, **13**, 5689–5696.
15 H. Li, T. Liu, P. Wei, L. Lin, D. Gao, G. Wang and X. Bao, *Angew. Chem., Int. Ed.*, 2021, **60**, 14329–14333.
16 M. Li, Y. Ma, J. Chen, R. Lawrence, W. Luo, M. Sacchi, W. Jiang and J. Yang, *Angew. Chem., Int. Ed.*, 2021, **60**, 11487–11493.
17 R. Chen, H.-Y. Su, D. Liu, R. Huang, X. Meng, X. Cui, Z.-Q. Tian, D. H. Zhang and D. Deng, *Angew. Chem., Int. Ed.*, 2020, **59**, 154–160.

18 Y. Wu, C. Chen, S. Liu, Q. Qian, Q. Zhu, R. Feng, L. Jing, X. Kang, X. Sun and B. Han, *Angew. Chem., Int. Ed.*, 2024, **63**, e202410659.
19 W. Wu, L. Luo, Z. Li, J. Luo, J. Zhao, M. Wang, X. Ma, S. Hu, Y. Chen and W. Chen, *Angew. Chem., Int. Ed.*, 2024, **136**, e202404983.
20 S. Li, G. Zhang, X. Ma, H. Gao, D. Fu, T. Wang, J. Zeng, Z.-J. Zhao, P. Zhang and J. Gong, *J. Am. Chem. Soc.*, 2024, **146**, 31927–31934.
21 Z. Wang, J. Guo, D. Wang, J. Ma, X. Feng, Z. Cui, D. Ruan, X. Luo, J. Fan, J. Yang, B.-Q. Xiong and X. Ren, *Angew. Chem., Int. Ed.*, 2026, **65**, e23475.
22 R. Dorakhan, I. Grigioni, B.-H. Lee, P. Ou, J. Abed, C. O'Brien, A. Sedighian Rasouli, M. Plodinec, R. K. Miao, E. Shirzadi, J. Wicks, S. Park, G. Lee, J. Zhang, D. Sinton and E. H. Sargent, *Nat. Synth.*, 2023, **2**, 448–457.
23 P. Zhu, C. Xia, C.-Y. Liu, K. Jiang, G. Gao, X. Zhang, Y. Xia, Y. Lei, H. N. Alshareef, T. P. Senftle and H. Wang, *Proc. Natl. Acad. Sci. U. S. A.*, 2021, **118**, e2010868118.
24 L. Zhang, J. Feng, R. Wang, L. Wu, X. Song, X. Jin, X. Tan, S. Jia, X. Ma, L. Jing, Q. Zhu, X. Kang, J. Zhang, X. Sun and B. Han, *J. Am. Chem. Soc.*, 2025, **147**, 713–724.
25 F. Ni, H. Yang, Y. Wen, H. Bai, L. Zhang, C. Cui, S. Li, S. He, T. Cheng, B. Zhang and H. Peng, *Sci. China Mater.*, 2020, **63**, 2606–2612.
26 H. Kang, L. Zhu, S. Li, S. Yu, Y. Niu, B. Zhang, W. Chu, X. Liu, S. Perathoner, G. Centi and Y. Liu, *Nat. Catal.*, 2023, **6**, 1062–1072.
27 K. Jenkinson, M. C. Spadaro, V. Golovanova, T. Andreu, J. R. Morante, J. Arbiol and S. Bals, *Adv. Mater.*, 2023, **35**, 2306447.
28 J. Feng, L. Zhang, S. Liu, L. Xu, X. Ma, X. Tan, L. Wu, Q. Qian, T. Wu, J. Zhang, X. Sun and B. Han, *Nat. Commun.*, 2023, **14**, 4615.
29 S. Li, G. Zhang, X. Ma, H. Gao, D. Fu, T. Wang, J. Zeng, Z.-J. Zhao, P. Zhang and J. Gong, *J. Am. Chem. Soc.*, 2024, **146**, 31927–31934.
30 C. Du, J. P. Mills, A. G. Yohannes, W. Wei, L. Wang, S. Lu, J.-X. Lian, M. Wang, T. Guo, X. Wang, H. Zhou, C.-J. Sun, J. Z. Wen, B. Kendall, M. Couillard, H. Guo, Z. Tan, S. Siahrostami and Y. A. Wu, *Nat. Commun.*, 2023, **14**, 6142.
31 D. Cheng, Z. Wei and P. Sautet, *J. Am. Chem. Soc.*, 2025, **147**, 10954–10965.
32 Q. Wu, Y. Li, Y. Cao, J. Li, J. Mao, X. Liu, W. Qu, P. Yan, Z. Cai, H. Lv, Y. Huang and Q. Li, *Angew. Chem., Int. Ed.*, 2026, **138**, e17120.
33 G. Wang, Y. Liu, X. Zhang, X. Zong, X. Zhang, K. Zheng, D. Qu, L. An, X. Qi and Z. Sun, *J. Am. Chem. Soc.*, 2024, **146**, 8668–8676.
34 Y. Dai, H. Li, C. Wang, W. Xue, M. Zhang, D. Zhao, J. Xue, J. Li, L. Luo, C. Liu, X. Li, P. Cui, Q. Jiang, T. Zheng, S. Gu, Y. Zhang, J. Xiao, C. Xia and J. Zeng, *Nat. Commun.*, 2023, **14**, 3382.
35 P. Wei, D. Gao, T. Liu, H. Li, J. Sang, C. Wang, R. Cai, G. Wang and X. Bao, *Nat. Nanotechnol.*, 2023, **18**, 299–306.
36 Y. Rong, T. Liu, J. Sang, R. Li, P. Wei, H. Li, A. Dong, L. Che, Q. Fu, D. Gao and G. Wang, *Angew. Chem., Int. Ed.*, 2023, **62**, e202309893.
37 Y. Rong, X. Guo, G. Zhang, J. Sang, H. Li, D. Gao and G. Wang, *ACS Energy Lett.*, 2024, **9**, 3204–3211.
38 S. Roy, Z. Li, Z. Chen, A. C. Mata, P. Kumar, S. C. Sarma, I. F. Teixeira, I. F. Silva, G. Gao, N. V. Tarakina, M. G. Kibria, C. V. Singh, J. Wu and P. M. Ajayan, *Adv. Mater.*, 2024, **36**, 2300713.
39 L. Liu, J. Hu, Y. Sheng, H. Akhoundzadeh, W. Tu, W. J. S. Siow, J. H. Ong, H. Huang and R. Xu, *ACS Nano*, 2024, **18**, 26271–26280.
40 H. Cheng, X. Wu, X. Li, X. Nie, S. Fan, M. Feng, Z. Fan, M. Tan, Y. Chen and G. He, *Chem. Eng. J.*, 2021, **407**, 126842.
41 K. Lee, E. J. Kim, J. Kim, K. H. Kim, Y. J. Lee, M. J. Lee, K. Ryu, S. Shin, J. Choi, S. H. Kwon, H. Lee, J. K. Kim, B.-H. Kim, B. J. Kim and S. W. Lee, *Adv. Energy Mater.*, 2024, **14**, 2303803.
42 C. Zhan, F. Dattila, C. Rettenmaier, A. Herzog, M. Herran, T. Wagner, F. Scholten, A. Bergmann, N. López and B. Roldan Cuenya, *Nat. Energy*, 2024, **9**, 1485–1496.
43 R. M. Arán-Ais, F. Scholten, S. Kunze, R. Rizo and B. Roldan Cuenya, *Nat. Energy*, 2020, **5**, 317–325.
44 Y. Liu, X. Wang, Z. Wang, C. Chen, J. Song, L. Zhang, W. Bao, B. Sun, L. Wang and D. Liu, *ACS Catal.*, 2024, **14**, 12610–12622.
45 Y. Yang, J. Zhang, Z. Tan, J. Yang, S. Wang, M. Li and Z. Su, *Angew. Chem., Int. Ed.*, 2024, **136**, e202408873.
46 T. Hou, J. Zhu, H. Gu, X. Li, Y. Sun, Z. Hua, R. Shao, C. Chen, B. Hu, L. Mai, S. Chen, D. Wang and J. Zhang, *Angew. Chem., Int. Ed.*, 2025, **137**, e202424749.
47 B. M. Tackett, D. Raciti, A. R. Hight Walker and T. P. Moffat, *J. Phys. Chem. Lett.*, 2021, **12**, 10936–10941.
48 R. Chen, Q. Wu, J. Zhu, S. Wang, Z. Hu, J. Hu, J. Zhu, H. Zhang, B. Ye, Y. Sun and Y. Xie, *J. Am. Chem. Soc.*, 2025, **147**, 7921–7931.
49 X. Guo, T. Liu, Y. Song, R. Li, P. Wei, Z. Liao, Z. Wu, D. Gao, Q. Fu, G. Wang and X. Bao, *Angew. Chem., Int. Ed.*, 2025, **64**, e202507062.
50 H. Matsushima, C. Haak, A. Taranovskyy, Y. Gründer and O. M. Magnussen, *Phys. Chem. Chem. Phys.*, 2010, **12**, 13992–13998.
51 X. Huang, H. Yao, Y. Cui, W. Hao, J. Zhu, W. Xu and D. Zhu, *ACS Appl. Mater. Interfaces*, 2017, **9**, 40752–40759.
52 Y. Qin, C. Xia, T. Wu, J. Zhang, G. Gao, B. Y. Xia, M. L. Coote, S. Ding and Y. Su, *J. Am. Chem. Soc.*, 2024, **146**, 32539–32549.
53 J. Sang, T. Liu, P. Wei, H. Li, C. Liu, Y. Wang, Y. Rong, Q. Wang, G. Wang and X. Bao, *Energy Environ. Sci.*, 2024, **17**, 3594–3603.